69th International Astronautical Congress (IAC), Bremen, Germany, 1-5 October 2018.

IAC-18,A6,10-C1.7,11,x45107

Dynamical system description of the solar radiation pressure and J_2 phase space for end-of-life design and frozen orbit design

Elisa Maria Alessi[a]*, Camilla Colombo[b]

[a] *Istituto di Fisica Applicata "Nello Carrara" – Consiglio Nazionale delle Ricerche (IFAC-CNR), Via Madonna del Piano 10, 50019 Sesto Fiorentino (FI), Italy,* em.alessi@ifac.cnr.it
[b] *Department of Aerospace Science and Technology, Politecnico di Milano, Via Giuseppe La Masa 34, 20156 Milano, Italy* camilla.colombo@polimi.it
* Corresponding Author

Abstract

In this work we review the effect of solar radiation pressure on the eccentricity of circumterrestrial orbits, perturbed also by the oblateness of the Earth. We compute the equilibrium points of a reduced system of equations describing the time evolution of the eccentricity, the longitude of the ascending node and the argument of pericenter, and their linear stability. This analysis is the basis for understanding how the phase space is organized in terms of central and hyperbolic orbits. The role of the initial phase with respect to the Sun and of the magnitude of the inclination evolution is also examined. The results follow previous investigations performed by the authors, providing a more complete picture of the whole dynamics, that can be applied to design convenient end-of-life strategies for small satellites equipped with a solar sail or to determine quasi stable Sun-following orbits for satellites swarms.

1. Introduction

The idea of this work stems from the will of finding a unique description of the dynamics induced by Solar Radiation Pressure (SRP) coupled with the oblateness of the Earth. In the past, the long-term variation in orbital elements due to this kind of perturbation was faced by different authors and the main effect in eccentricity was described in terms of either resonances or dynamics associated with equilibrium points.

The pioneers in the identification of the role of SRP coupled with J_2 in the orbital evolution were Musen [1] and Cook [2], who developed the corresponding singly-averaged equations of motion, for a satellite orbiting the Earth, in terms of Keplerian orbital elements, and remarked the existence of six resonances. Later on, Hughes [3] expanded the disturbing function associated with SRP using the Kaula's method up to high order terms, and provided some examples on whether they can be relevant for Earth satellites. Breiter [4, 5] addressed the analytical treatment of the perturbation in canonical coordinates, starting from a general description concerning luni-solar perturbations.

The effect of the solar radiation pressure coupled with the oblateness of a planet was also extensively studied in the vast literature on the dynamics of dust in planetary systems. Among them, Krivov et al. [6] and Hamilton and Krivov [7] wrote the dynamics in a Hamiltonian form considering the singly-averaged disturbing potential of SRP and J_2 for a dust particle around a planet and studied the eccentricity oscillations. Krivov and Getino [8] applied the same model for obtaining a graphical and analytical phase-space representation of the orbit evolution in the eccentricity and the resonant angle for low-inclination orbits and applied it to study the dynamics of high-altitude balloons. Colombo et al. [9] performed a parametric analysis of the SRP-J_2 phase-space for different values of semi-major axis and area-to-mass ratio identifying the equilibrium conditions for frozen orbits which maintains constant their apses orientation with respect to the Sun, either heliotropic (apogee pointing towards the Sun) or anti-heliotropic (perigee pointing towards the Sun) orbits. The in-plane equilibrium conditions where numerically extended for non-zero inclinations. Different applications were proposed for these equilibrium

points, such as the use of heliotropic orbits for Earth observation in the visible wavelength [9, 10], or the use of heliotropic orbits at an oblate asteroid [11], or also the use of anti-heliotropic orbits for geomagnetic tail exploration missions [12, 13, 14].

In general, also the contour lines of the Hamiltonian of the SRP-J_2 phase space, not necessarily corresponding to equilibria, have some interesting applications due to their natural evolution, such as the study of planetary dynamics [6], the evolution of a swarm of satellites-on-a-chip or a cloud of debris fragments [15, 16]. Following the work of Krivov and Getino [8] a particular application of this dynamics was proposed by Lücking at al. [17, 18] for passive deorbing of spacecraft at the end-of-life. The area-to-mass ratio of the spacecraft can be deliberately increased, by deploying a solar sail, at the end-of-life of the satellite. In this way, the eccentricity of the orbit will undergo large oscillation that can bring the orbit perigee to enter in the drag-dominated region and therefore to reach reentry through the enhancement of the natural perturbation. The requirements in terms of sail area for a given semi-major axis and inclination were computed in [17, 18] by studying the phase space line of the SRP-J_2 Hamiltonian originating from circular orbits and computing the maximum attainable eccentricity for a given value of the area-to-mass ratio. The time required for deorbit was also considered in the optimization process; therefore, in the case of deorbiting through a hyperbolic equilibrium point, the area-to-mass ratio was increased with respect to the minimum possible, to have a bounded value of the deorbiting time. Later on in [19] the requirements in terms of area-to-mass ratio were computed for many values of the initial altitudes and inclinations of a circular to elliptical orbit through a numerical technique.

With the same aim of looking for natural perturbations which can support a reentry from Low Earth Orbits (LEO) at the end-of-life, Alessi et al. [20] performed an extensive numerical mapping of the region and identified natural dynamical corridors in inclination-eccentricity for given semi-major axis which can be exploited with the aid of an area-enhancing device. In [21], the same authors compared the effect in eccentricity detected numerically, for the six main SRP resonances, with the maximum variation in eccentricity which can be predicted analytically starting from the corresponding Lagrange planetary equations. The width of the resonances was also computed, following [22]. In [23], a numerical frequency portrait of the LEO region is presented, highlighting also the role that high-order resonances associated with SRP [3] might have.

Table 1: Argument $\psi_j = n_1\Omega + n_2\omega + n_3\lambda_S$ of the periodic component in terms of n_1, n_2, n_3.

j	n_1	n_2	n_3
1	1	1	-1
2	1	-1	-1
3	0	1	-1
4	0	1	1
5	1	1	1
6	1	-1	1

In this work, the three-dimensional equations of motion which describe the variation in eccentricity, inclination, and a given angle accounting for the motion of the longitude of the ascending node and the argument of pericenter are analyzed, and the concept of resonance is linked with the one of equilibrium point. The corresponding stability is provided for the six main resonances and the possible different phase space portraits are presented to introduce their exploitation for mission design and end-of-life purposes.

2. Dynamical Model

Let us assume that the spacecraft moves under the effect of the Earth's monopole, the Earth's oblateness and the SRP. In particular, for the SRP the so-called cannonball model is used, the orbit of the spacecraft is entirely in sunlight and the effect of the Earth's albedo is negligible.

In the following, we denote as P the solar radiation pressure, c_R the reflectivity coefficient, taken equal to 1 in this work, A/m the area-to-mass ratio of the spacecraft, $(a, e, i, \Omega, \omega)$ the Keplerian orbital elements measured with respect to the Earth equatorial plane, n the mean motion of the spacecraft, λ_S the longitude of the Sun measured on the ecliptic plane, J_2 the second zonal term of the geopotential and $r_\oplus$ the equatorial radius of the Earth.

Under these hypotheses and notations, following the description given in [6, 21], if $C_{SRP} = \frac{3}{2} P c_R \frac{A}{m}$ and

$$\psi_j = n_1\Omega + n_2\omega + n_3\lambda_S, \tag{1}$$

with n_1, n_2, n_3 as in Table 1, the singly-averaged equations of motion of the spacecraft can be writ-

ten as

$$\begin{aligned}
\frac{da}{dt} &= 0,\\
\frac{de}{dt} &= -C_{SRP}\frac{\sqrt{1-e^2}}{na}\sum_{j=1}^{6}\mathcal{T}_j\frac{\partial\cos\psi_j}{\partial\omega}, \qquad (2)\\
\frac{di}{dt} &= -C_{SRP}\frac{e}{na\sqrt{1-e^2}\sin i}\sum_{j=1}^{6}\mathcal{T}_j\times\\
&\quad\times\left(\frac{\partial\cos\psi_j}{\partial\Omega}-\cos i\frac{\partial\cos\psi_j}{\partial\omega}\right),\\
\frac{d\Omega}{dt} &= \dot{\Omega}_{J_2}+\dot{\Omega}_{SRP},\\
\frac{d\omega}{dt} &= \dot{\omega}_{J_2}+\dot{\omega}_{SRP},
\end{aligned}$$

where

$$\begin{aligned}
\mathcal{T}_1 &= \cos^2\left(\frac{\epsilon}{2}\right)\cos^2\left(\frac{i}{2}\right),\\
\mathcal{T}_2 &= \cos^2\left(\frac{\epsilon}{2}\right)\sin^2\left(\frac{i}{2}\right),\\
\mathcal{T}_3 &= \frac{1}{2}\sin(\epsilon)\sin(i), \qquad (3)\\
\mathcal{T}_4 &= -\frac{1}{2}\sin(\epsilon)\sin(i),\\
\mathcal{T}_5 &= \sin^2\left(\frac{\epsilon}{2}\right)\cos^2\left(\frac{i}{2}\right),\\
\mathcal{T}_6 &= \sin^2\left(\frac{\epsilon}{2}\right)\sin^2\left(\frac{i}{2}\right),
\end{aligned}$$

and

$$\begin{aligned}
\dot{\Omega}_{J_2} &= -\frac{3}{2}\frac{J_2 r_\oplus^2 n}{a^2(1-e^2)^2}\cos i, \qquad (4)\\
\dot{\Omega}_{SRP} &= C_{SRP}\frac{e}{na\sqrt{1-e^2}\sin i}\sum_{j=1}^{6}\frac{\partial\mathcal{T}_j}{\partial i}\cos\psi_j,\\
\dot{\omega}_{J_2} &= \frac{3}{4}\frac{J_2 r_\oplus^2 n}{a^2(1-e^2)^2}\left(5\cos^2 i-1\right),\\
\dot{\omega}_{SRP} &= C_{SRP}\frac{\sqrt{1-e^2}}{nae}\sum_{j=1}^{6}\mathcal{T}_j\cos\psi_j-\dot{\Omega}_{SRP}\cos i.
\end{aligned}$$

If we assume that the dynamics is driven by a single term j at a time, that means that only one periodic component $\sin\psi_j$ (for e, i; $\cos\psi_j$ for Ω, ω) affects the motion at a time, then we can simplify the description of the dynamics by analyzing the following system

$$\begin{aligned}
\left.\frac{de}{dt}\right|_j &= n_2 C_{SRP}\frac{\sqrt{1-e^2}}{na}\mathcal{T}_j\sin\psi_j, \qquad (5)\\
\frac{d\psi_j}{dt} &= n_1\dot{\Omega}_{(J_2,j)}+n_2\dot{\omega}_{(J_2,j)}+n_3 n_S,
\end{aligned}$$

where n_S is the apparent mean motion of the Sun, and $\dot{\Omega}_{(J_2,j)}$ and $\dot{\omega}_{(J_2,j)}$ are intended to include the contribution of J_2 and the j contribution of the SRP. In the following treatment, $\left.\frac{de}{dt}\right|_j$ will appear as $\dot{e}_{|j}$.

According to [22], the behavior in inclination can be recovered at any time by means of the integral of motion

$$\Lambda = (n_2\cos i - n_1)\sqrt{\mu a(1-e^2)}, \qquad (6)$$

where μ is the gravitational constant of the Earth. Eq. (6) can be inverted to get

$$\cos i = \frac{\Lambda}{n_2\sqrt{\mu a(1-e^2)}}+\frac{n_1}{n_2}. \qquad (7)$$

Note that the evolution of the dynamics is determined by three parameters, the semi-major axis a, the area-to-mass ratio A/m and the integral of motion Λ. For resonance, we mean that the following condition is satisfied

$$\dot{\psi}_j \approx 0. \qquad (8)$$

Note that Eq. (8) depends on (a, e, i, ψ_j).

If, at the same time, the first equation in Eqs. (5) cancels out, then an equilibrium point is computed. This must happen in particular at $\psi_j = 0$ or $\psi_j = \pi$.

The stability of the points can be evaluated by computing the eigenvalues of the matrix

$$\begin{pmatrix} \frac{\partial\dot{e}_{|j}}{\partial e} & \frac{\partial\dot{e}_{|j}}{\partial\psi_j}\\ \frac{\partial\dot{\psi}_j}{\partial e} & \frac{\partial\dot{\psi}_j}{\partial\psi_j}\end{pmatrix},$$

at the given equilibrium point, where

$$\begin{aligned}
\frac{\partial\dot{e}_{|j}}{\partial e} &= 0,\\
\frac{\partial\dot{e}_{|j}}{\partial\psi_j} &= n_2 C_{SRP}\frac{\sqrt{1-e^2}}{na}\mathcal{T}_j\cos\psi_j,\\
\frac{\partial\dot{\psi}_j}{\partial e} &= n_1\frac{\partial\dot{\Omega}_{(J_2,j)}}{\partial e}+n_2\frac{\partial\dot{\omega}_{(J_2,j)}}{\partial e}, \qquad (9)\\
\frac{\partial\dot{\psi}_j}{\partial\psi_j} &= 0.
\end{aligned}$$

To calculate the third of Eqs. (9), taking into

account Eq. (7), we can write

$$\begin{aligned}
\frac{\partial \dot{\Omega}_{(J_2,j)}}{\partial e} &= -6\frac{J_2 r_\oplus^2 n e}{a^2(1-e^2)^3}\cos i \; + \\
&\frac{C_{SRP}}{na(1-e^2)^{3/2}\sin i}\frac{\partial \mathcal{T}_j}{\partial i}\cos\psi_j \; + \\
&-\frac{3}{2}\frac{J_2 r_\oplus^2 n}{a^2(1-e^2)^2}\frac{\partial \cos i}{\partial e} \; + \\
&C_{SRP}\frac{e}{na\sqrt{1-e^2}}\frac{\partial \mathcal{T}_j}{\partial i}\cos\psi_j \frac{\partial}{\partial e}\frac{1}{\sin i} \; + \\
&C_{SRP}\frac{e}{na\sqrt{1-e^2}\sin i}\cos\psi_j \frac{\partial}{\partial e}\frac{\partial \mathcal{T}_j}{\partial i}, \\
\frac{\partial \dot{\omega}_{(J_2,j)}}{\partial e} &= 3\frac{J_2 r_\oplus^2 n e}{a^2(1-e^2)^3}(5\cos^2 i - 1) \; - \\
&\frac{C_{SRP}}{na\sqrt{1-e^2}}\left(\frac{\mathcal{T}_j}{e^2} - \frac{\cos i}{(1-e^2)^2\sin i}\frac{\partial \mathcal{T}_j}{\partial i}\right)\cos\psi_j + \\
&\frac{15}{2}\frac{J_2 r_\oplus^2 n\cos i}{a^2(1-e^2)^2}\frac{\partial \cos i}{\partial e} \; + \\
&C_{SRP}\frac{\sqrt{1-e^2}}{nae}\cos\psi_j \frac{\partial \mathcal{T}_j}{\partial e} \; - \\
&C_{SRP}\frac{e}{na\sqrt{1-e^2}}\frac{\partial \mathcal{T}_j}{\partial i}\cos\psi_j \frac{\partial}{\partial e}\frac{1}{\tan i} \; + \\
&C_{SRP}\frac{e}{na\sqrt{1-e^2}\tan i}\cos\psi_j \frac{\partial}{\partial e}\frac{\partial \mathcal{T}_j}{\partial i},
\end{aligned}$$

where

$$\begin{aligned}
\frac{\partial \cos i}{\partial e} &= \frac{e\Lambda}{n_2\sqrt{\mu a}(1-e^2)^{3/2}}, \\
\frac{\partial \sin i}{\partial e} &= \frac{1}{\tan i}\frac{\partial \cos i}{\partial e},
\end{aligned}$$

and $\frac{\partial \mathcal{T}_j}{\partial i}$ and $\frac{\partial}{\partial e}\frac{\partial \mathcal{T}_j}{\partial i}$ can be derived from these expressions by applying the half-angle trigonometric formulae to Eqs. (3).

Given a value for the semi-major axis a^*, the eigenvalues $\lambda_{1,2}$ at a given equilibrium point (e^*, i^*, ψ^*) are thus determined by the condition

$$\lambda^2 - \left(\frac{\partial \dot{e}_{|j}}{\partial \psi_j}\right)\left(\frac{\partial \dot{\psi}_j}{\partial e}\right) = 0. \tag{10}$$

2.1 Resonances and Equilibrium Points

In Figs. 1–6, we show the values of eccentricity and inclination which correspond to the resonant condition $\dot{\psi}_j \approx 0$ for three different values of ψ_j, given semi-major axis and area-to-mass ratio. For the sake of conciseness, we limit the representation to $a = 9378$ km, but similar figures can be provided for the Medium Earth Orbits (MEO) and Geostationary Orbit (GEO) regions. The plots are obtained by assuming $\psi_j = 0$ (left) and $\psi_j = \pi$ (right), that is, they provide the location of the equilibrium points, but also assuming $\psi_j = \pi/2$ (middle), which, in turn, is equivalent to consider the rate of precession of Ω and ω independent to the SRP, but only due to J_2.

For the lowest value of area-to-mass ratio displayed, namely $A/m = 0.012$ m^2/kg, the curves computed at the three values of ψ_j do not manifest a meaningful variation one with respect the others. This is the case of a typical spacecraft, where the effect of SRP is negligible in $\dot{\Omega}$ and $\dot{\omega}$. Considering an area-augmentation device feasible with the current technologies, that is, $A/m = 1$ m^2/kg [24], in the case of $j = 1, 2$ the range of inclination corresponding to equilibrium points enlarges. The same is true for $j = 1, 2, 3, 4$ when $A/m = 20$ m^2/kg, a value that can be attributable to a high area-to-mass fragment.

Note that the first equation in (5) states that the steepest variation in eccentricity corresponds to the resonant condition computed at $\psi_j = \pi/2$ or $\psi_j = 3\pi/2$. In particular, we have the steepest increase for $j = 1, 3, 5$ at $\psi_j = \pi/2$, while for $j = 2, 4, 6$ at $\psi_j = 3\pi/2$. On the other side, the steepest decrease for $j = 1, 3, 5$ takes place at $\psi_j = 3\pi/2$, while for $j = 2, 4, 6$ it takes place at $\psi_j = \pi/2$.

In Figs. 7–8, we show the stability of the equilibrium points computed for the six resonances, assuming $A/m = 1$ m^2/kg. Note that to interpret them correctly (and exploit their information for practical applications), the information on the value of Λ corresponding to that equilibrium point must be taken into account. For instance, looking at Fig. 7 we can see that we have two stable equilibria at $e \approx 0.2$ for $a = 7378$ km[1], but they correspond to two different values of inclination, and, although the difference is low[2], the corresponding value of Λ is such that the object moves in two different regimes. We shall thus look to equilibrium points corresponding to the same value of Λ. Notice that it can happen that only one equilibrium exists for a given $(a, \Lambda, A/m)$. As an example, in Fig. 9 on the left, the phase portrait corresponding to $a = 7378$ km, $e = 0.2$, $i = 41.63°$ is shown, assuming that only resonance 1 dominates the dynamics and $A/m = 1$ m^2/kg. On the other hand, more than two equilibrium points can occur for a given $(a, \Lambda, A/m)$. An example is shown in Fig. 9 on the right, for $a = 8378$ km, $e = 0.13$, $i = 38.74°$ assuming that only resonance 1 dominates the dynamics and $A/m = 1$ m^2/kg.

The number of equilibrium points that can be

[1] Neglect for the moment the fact that these values are associated with a perigee below the surface of the Earth.

[2] For this specific example $i = 41.63°$ for the equilibrium at $\psi_1 = 0$ and $i = 41.46°$ for the equilibrium at $\psi_1 = \pi$.

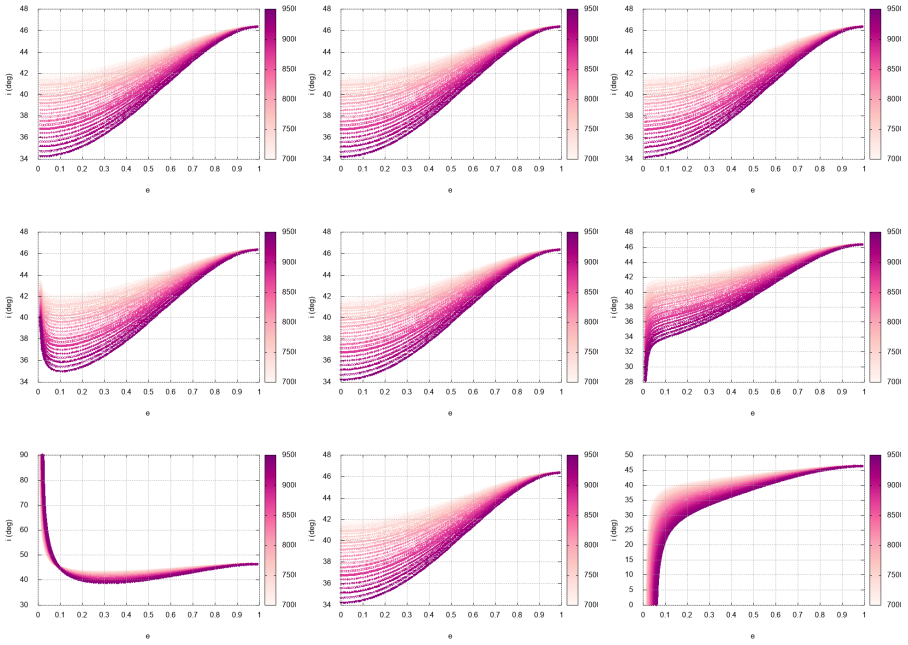

Figure 1: Eccentricity-inclination values corresponding to the resonant condition $\dot{\psi}_1 \approx 0$. The colorbar report the value of the semi-major axis, assumed here in an extended Low Earth Orbit (LEO) region. Left: $\psi_1 = 0$, middle: $\psi_1 = \pi/2$, right: $\psi_1 = \pi$. Top: $A/m = 0.012$ m^2/kg, center: $A/m = 1$ m^2/kg, bottom: $A/m = 20$ m^2/kg.

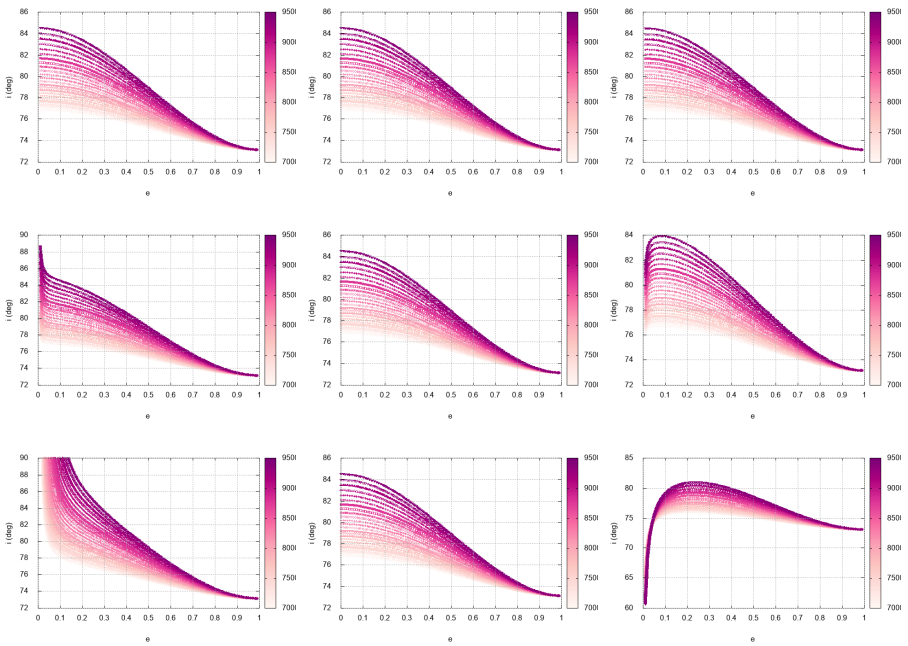

Figure 2: Eccentricity-inclination values corresponding to the resonant condition $\dot{\psi}_2 \approx 0$. The colorbar report the value of the semi-major axis, assumed here in an extended LEO region. Left: $\psi_2 = 0$, middle: $\psi_2 = \pi/2$, right: $\psi_2 = \pi$. Top: $A/m = 0.012$ m^2/kg, center: $A/m = 1$ m^2/kg, bottom: $A/m = 20$ m^2/kg.

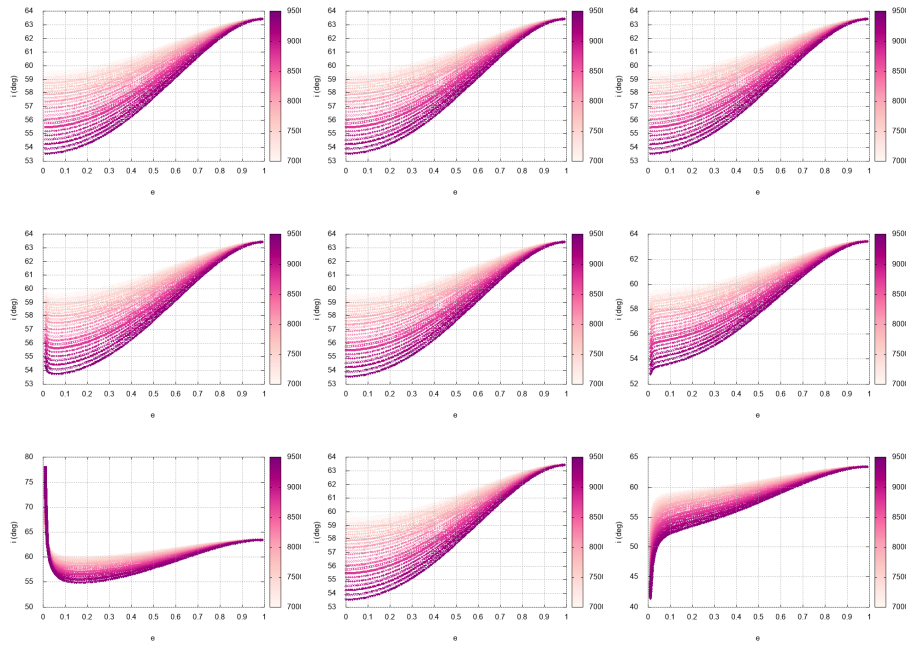

Figure 3: Eccentricity-inclination values corresponding to the resonant condition $\dot{\psi}_3 \approx 0$. The colorbar report the value of the semi-major axis, assumed here in an extended LEO region. Left: $\psi_3 = 0$, middle: $\psi_3 = \pi/2$, right: $\psi_3 = \pi$. Top: $A/m = 0.012$ m^2/kg, center: $A/m = 1$ m^2/kg, bottom: $A/m = 20$ m^2/kg.

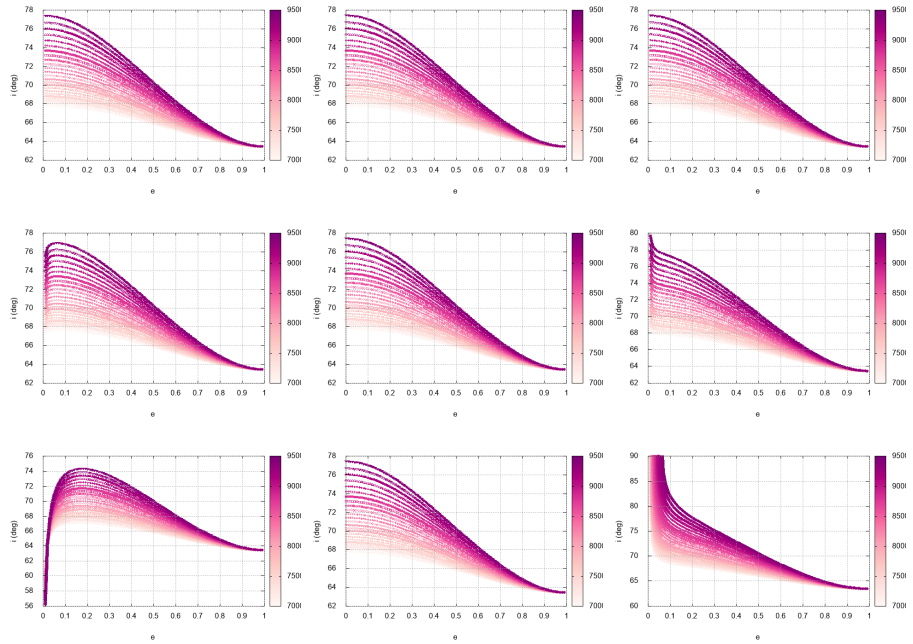

Figure 4: Eccentricity-inclination values corresponding to the resonant condition $\dot{\psi}_4 \approx 0$. The colorbar report the value of the semi-major axis, assumed here in an extended LEO region. Left: $\psi_4 = 0$, middle: $\psi_4 = \pi/2$, right: $\psi_4 = \pi$. Top: $A/m = 0.012$ m^2/kg, center: $A/m = 1$ m^2/kg, bottom: $A/m = 20$ m^2/kg.

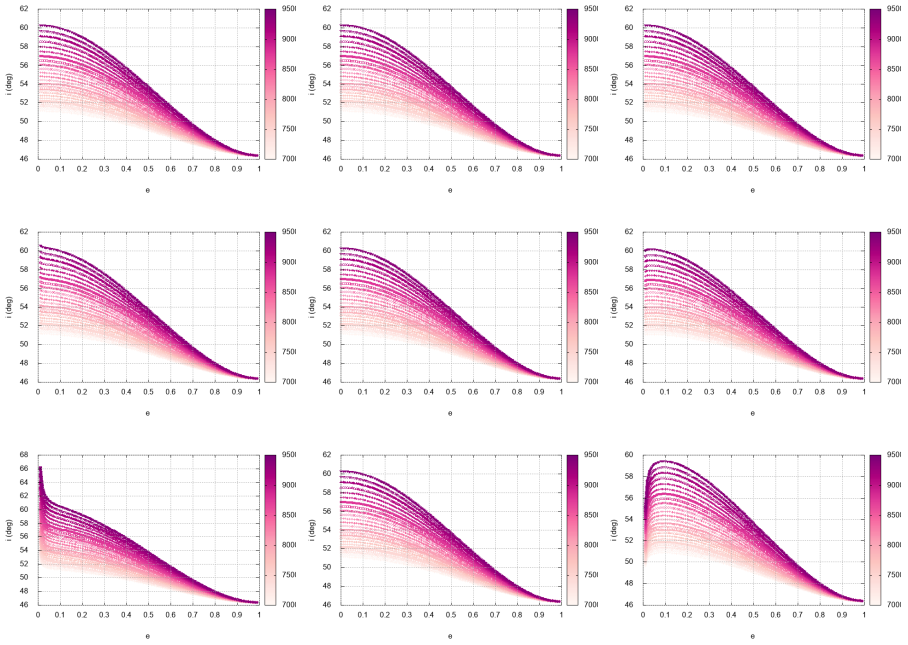

Figure 5: Eccentricity-inclination values corresponding to the resonant condition $\dot{\psi}_5 \approx 0$. The colorbar report the value of the semi-major axis, assumed here in an extended LEO region. Left: $\psi_5 = 0$, middle: $\psi_5 = \pi/2$, right: $\psi_5 = \pi$. Top: $A/m = 0.012$ m^2/kg, center: $A/m = 1$ m^2/kg, bottom: $A/m = 20$ m^2/kg.

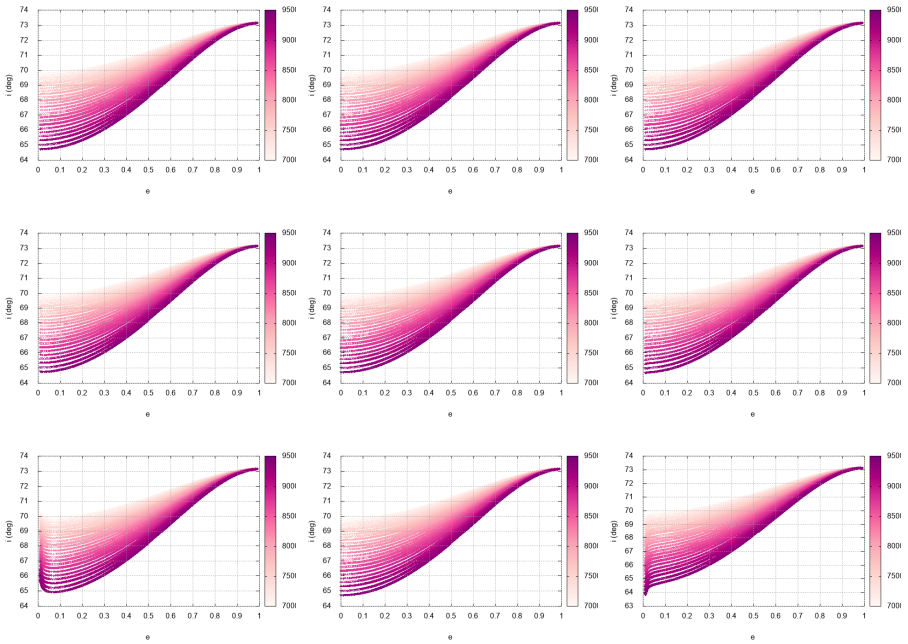

Figure 6: Eccentricity-inclination values corresponding to the resonant condition $\dot{\psi}_6 \approx 0$. The colorbar report the value of the semi-major axis, assumed here in an extended LEO region. Left: $\psi_6 = 0$, middle: $\psi_6 = \pi/2$, right: $\psi_6 = \pi$. Top: $A/m = 0.012$ m^2/kg, center: $A/m = 1$ m^2/kg, bottom: $A/m = 20$ m^2/kg.

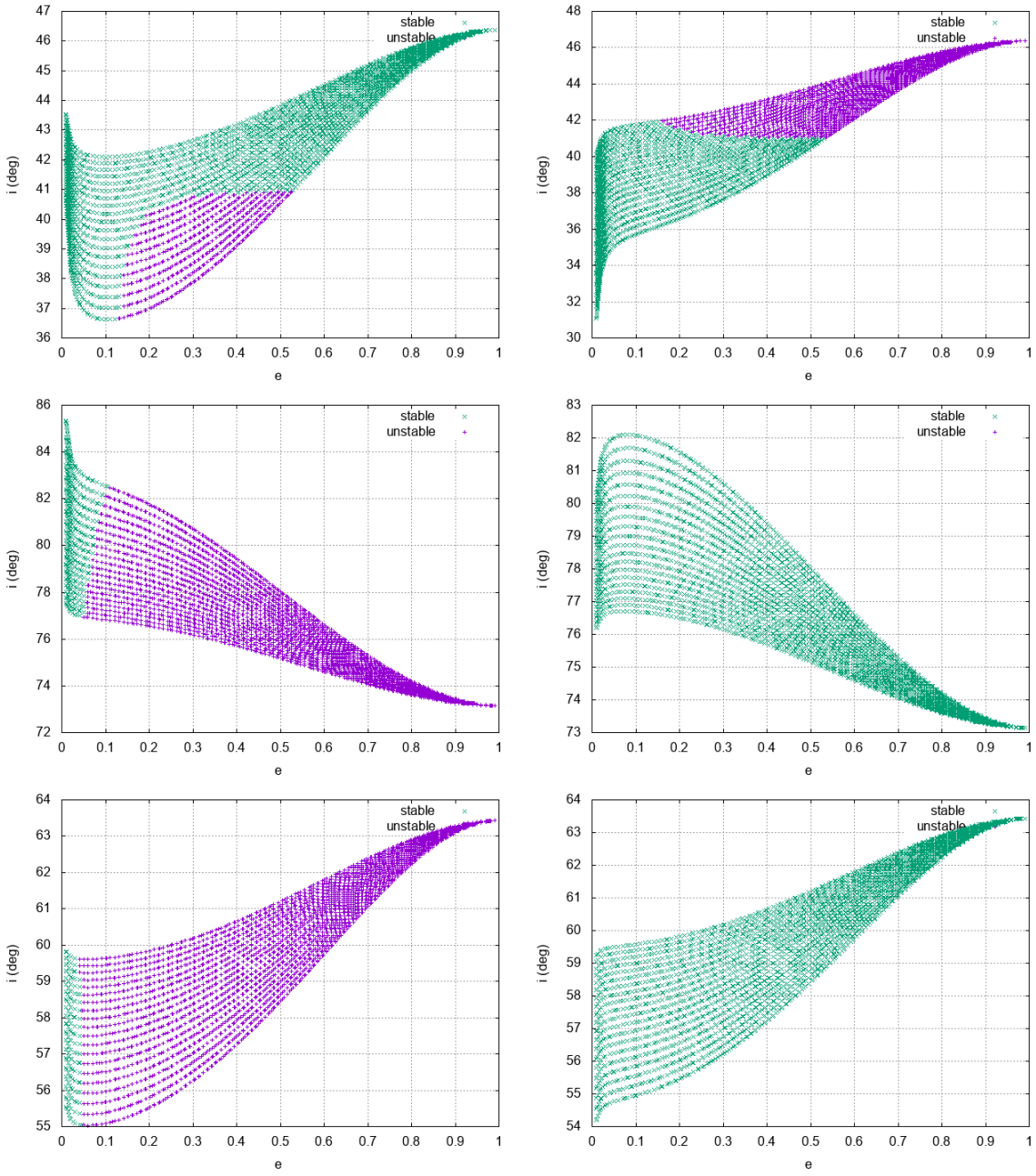

Figure 7: Eccentricity-inclination values corresponding to the resonant condition $\dot{\psi}_1 \approx 0$ (top), $\dot{\psi}_2 \approx 0$ (middle) and $\dot{\psi}_3 \approx 0$ (bottom), along with their stability character for the values of semi-major axis considered in Fig. 6 and $A/m = 1$ m^2/kg. Left: $\psi_j = 0$, right: $\psi_j = \pi$. Green: stable; purple: unstable.

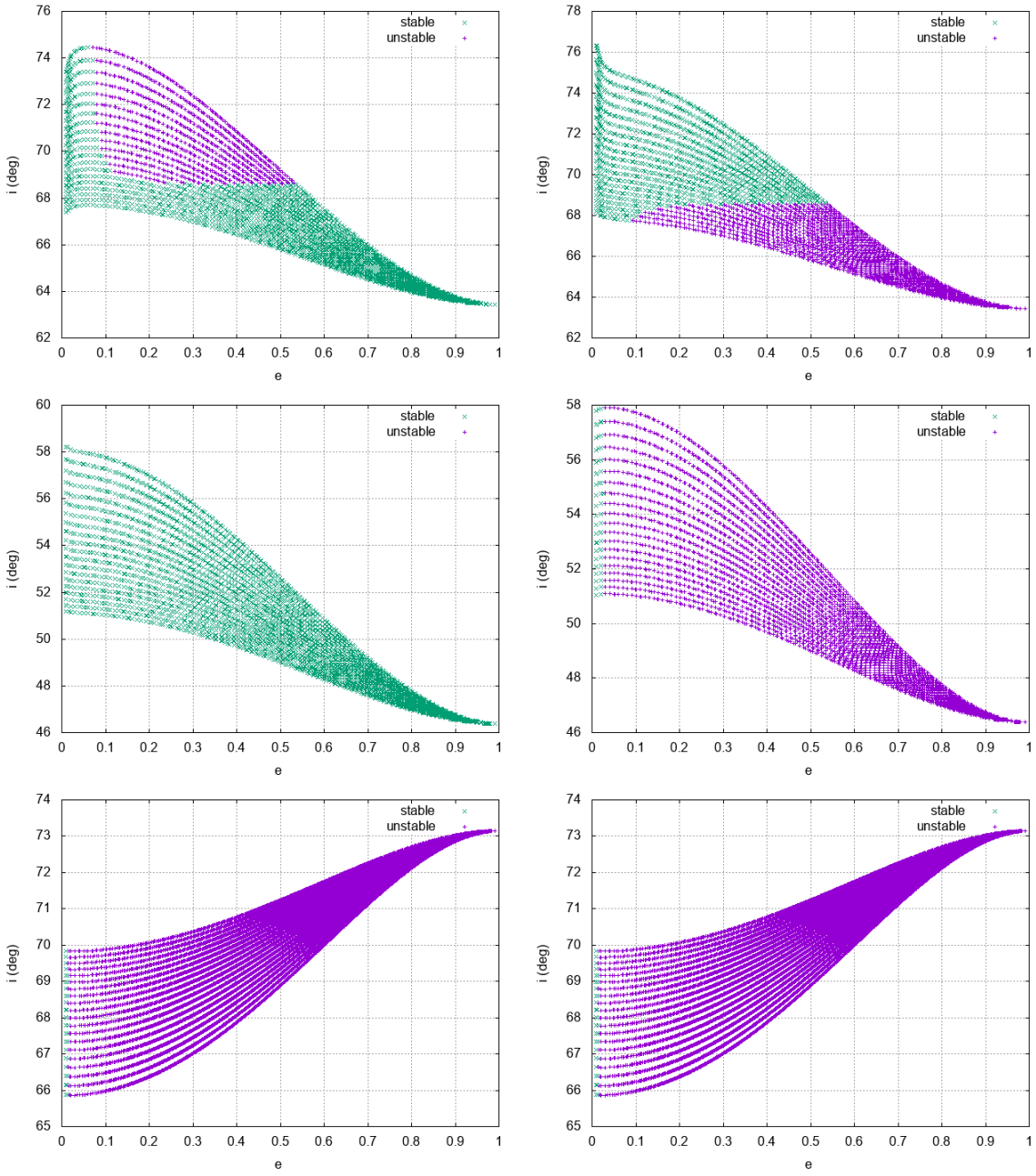

Figure 8: Eccentricity-inclination values corresponding to the resonant condition $\dot{\psi}_4 \approx 0$ (top), $\dot{\psi}_5 \approx 0$ (middle) and $\dot{\psi}_6 \approx 0$ (bottom), along with their stability character for the values of semi-major axis considered in Fig. 6 and $A/m = 1$ m^2/kg. Left: $\psi_j = 0$, right: $\psi_j = \pi$. Green: stable; purple: unstable.

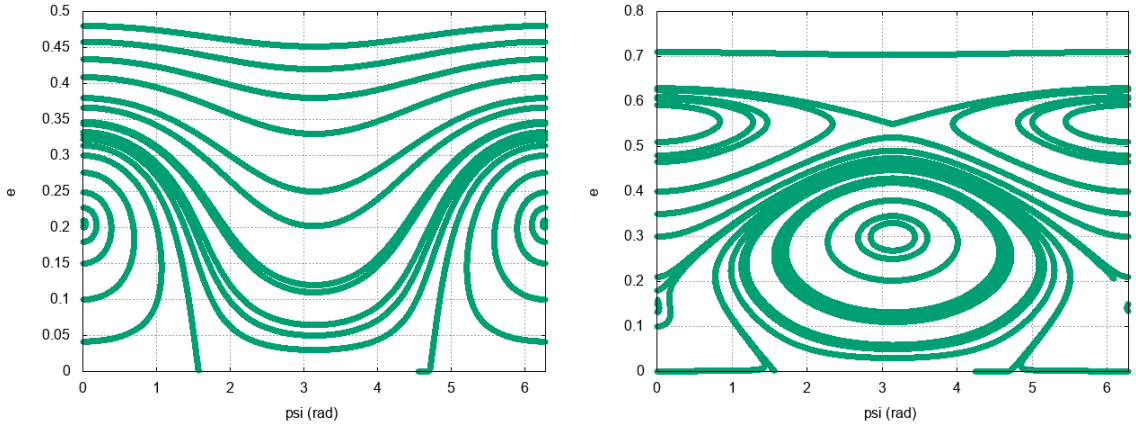

Figure 9: Phase portrait corresponding to Λ computed at $a = 7378$ km, $e = 0.2$, $i = 41.63°$ (left) and $a = 8378$ km, $e = 0.13$, $i = 38.74°$ (left), assuming that only resonance 1 dominates the dynamics and $A/m = 1$ m^2/kg.

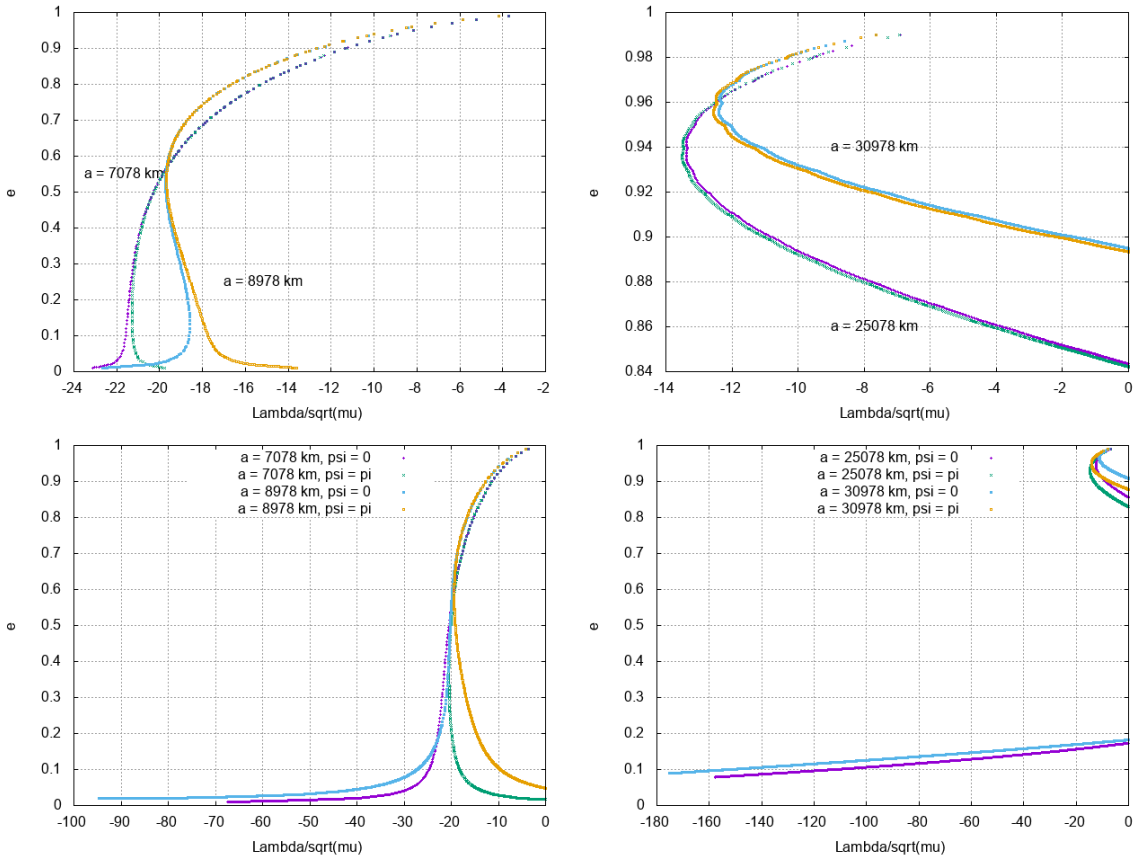

Figure 10: Equilibria location for resonance 1 for two different values of semi-major axis in the LEO (left) and in the MEO (right) region, as a function of $(\Lambda/\sqrt{\mu}, e)$. Top: $A/m = 1$ m^2/kg. Bottom: $A/m = 20$ m^2/kg.

obtained for a given value of $(a, \Lambda, A/m)$ can be derived by looking to the behaviour of the curves like the ones in Fig. 10, which are analogous to Fig. 7 except that instead of the inclination, the value of Λ is represented in the x-axis. For a given Λ, the number of intersections with the two curves gives the number of the equilibrium points. Notice that, when the curves are parallel, to the y-axis, it corresponds to the case where two coincident equilibria exists with a different stability property, for example the stable and the unable equilibrium at the same value of ψ coexist for the same $(a, \Lambda, A/m)$.

On the other hand, the representation in (e, i) as in Figs. 7–8 shows the range of inclination, for given area-to-mass ratio and semi-major axis, for which the central and hyperbolic dynamics can be exploited. In other words, for given $(a, A/m)$ and resonance j, outside the inclination range displayed the motion is of pure circulation.

These results for $i = 0$ are in agreement with the one of [9]; in that work the stable and unstable equilibrium points for $\psi = 0$ and $\psi = \pi$[3] where computed, for different values of e, a and A/m. As visible in Figure 3 of [9], for small semi-major axis (on the x-label) only the equilibrium at $\psi = \pi$ ($\phi = 0$), exists at a given eccentricity. For higher values of the semi-major axis two equilibria at $\psi = 0$ ($\phi = \pi$) appears, one stable, one unstable. When the dashed and dotted line coincides (see dot symbol, the stable and the unstable equilibrium coincides).

3. Applications

We present two examples of application of the dynamical description given above.

3.1 Deorbiting Strategies

The first application is the design of a deorbiting strategy. As a matter of fact, the natural SRP perturbation coupled with J_2 can be exploited to increase the eccentricity as much as to reenter. This was firstly proposed by Lücking at al. [17, 18] where the requirements in terms of A/m for deorbiting were derived from the phase space representation (like the one in Fig. 9) studying the phase space line in correspondence of the initial condition at $\psi = \pi/2$ or $\psi = 3\pi/2$ and $e = 0$. In that work an analytical solution was found for planar orbits. For initially inclined orbits, instead, a continuation method, together with a zero-solver were used as explained in [19]. The phase space analysis presented in Section 2.1 can be used in the same way for finding the A/m requirements for deorbiting from inclined orbits.

Let us consider, as an example, a quasi-circular orbit, say $e = 0.001$ at $a = 7578$ km, and assume that the mass of the satellite is such that it is allowed to enhance its area-to-mass ratio up to 1 m^2/kg with a sail. In Fig. 11, we show the location of the equilibrium points as a function of (i, e) under the above hypotheses. The resonance computed at $\psi_j = \pi/2$ (not shown in the figure) lies in between the $\psi_j = 0$ and $\psi_j = \pi$ curves. Note that the value of semi-major axis and eccentricity considered simulates the ones of the upcoming large constellations.

As noticed before, the figure shows, first of all, the range of inclination where the SRP can be exploited to deorbiting. Each inclination of interest, that is, resonance, yields, however, a different change in eccentricity. The largest variation for quasi-circular orbits corresponds to $\psi_j = \pi/2$ or $\psi_j = 3\pi/2$, depending on the resonance.

Given the inclination (or the resonance j and Λ), the maximum eccentricity that can be achieved, starting from $\psi_j = \pi/2 + k\pi$ ($k \in \mathbb{Z}$), corresponds to the values (ψ_j, e) satisfying the conditions

$$\begin{aligned} \dot{e}_{|j} &= 0 \\ \frac{d\dot{e}_{|j}}{dt} &= n_2 C_{SRP} \frac{\sqrt{1-e^2}}{na} \mathcal{T}_j \dot{\psi}_j \cos\psi_j < 0. \end{aligned} \tag{11}$$

Notice that the second derivative $\frac{d\dot{e}_{|j}}{dt}$ written assumes that the maximum occurs at either $\psi_j = 0$ or $\psi_j = \pi$.

For the example considered, we write in Tab. 2 the initial conditions of departure for deorbiting following the steepest increase in eccentricity, the (ψ_j, e) conditions corresponding to the maximum and the time needed to get there. These values are computed numerically on the basis of Eqs. (11), Eqs. (5), Eq. (7). Notice that in all the cases, except for resonance 4 (see Fig. 12), there exists only one equilibrium point corresponding to the given Λ. Given the results obtained in [20], it is possible to deorbit by exploiting any of the first three resonances. In particular from [20], for resonance 1 the spacecraft will reenter directly once reached the value $e = 0.145$, while for resonance 2 and 3 it will deorbit naturally by the effect of the atmospheric drag. For resonance 2, this will take an additional amount of about 10 years without the aid of the sail,

[3] In [9] it is used $\phi = \Omega + \omega - \lambda_S + \pi$ so that so that $\phi = \psi_1 + \pi$ following the notation of the current paper.

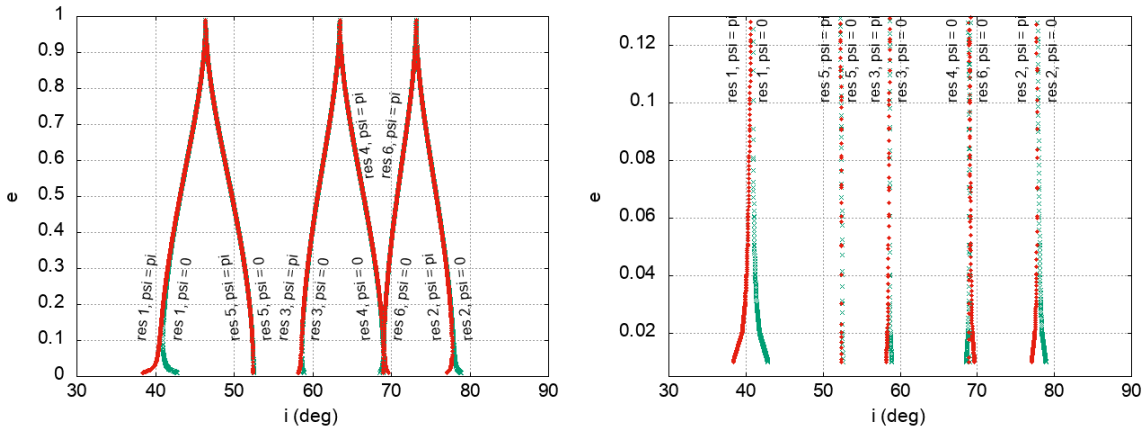

Figure 11: Inclination-eccentricity location of the equilibrium points for $a = 7578$ km and $A/m = 1$ m^2/kg. On the right, a close view for feasible values of eccentricity.

for resonance 3 the sail shall remain open. Notice that, looking at Figure 4 in [19], when one of these resonances is exploited, the requirements in terms of area-to-mass ratio for deorbiting are small.

From the point of view of the mission design, the example shows that to place the satellites in the neighborhood of any of the three values of inclination i_0 for $j = 1, 2, 3$ will facilitate the end-of-life procedures. Hence, it is recommendable to see if the operational requirements can be met at any of these inclinations.

On the other hand, it shall be noted that a reentry can be accomplished also if the spacecraft does not move along the curve starting from $e \approx 0$ and $\psi_j = \pi/2 + k\pi$ $(k = 1, 2)$, like the red one in Fig. 12. This is, an eccentricity variation high enough to achieve reentry can be attained also along the libration curves associated with the elliptic equilibrium point. In this case, the required area-to-mass with be slightly higher than the minimum one required, or equivalently a small manoeuvre will be required to achieve the initial condition of deorbiting, but the total reentry time will be reduced [19].

3.2 Bounded Motion for geomagnetic tail exploration mission

As an additional application, the equilibrium conditions in Figs. 1–6 and Fig. 10 can be used for identifying frozen heliotropic or anti-heliotropic orbit as done in [9] and [10]. For example a mission to study the geomagnetic tail can be designed as proposed in [12, 13, 14].

Figure 13 shows the location of the anti-heliotropic equilibrium points for planar and inclined orbits in the (e, i) space for different values of the semi-major axis in the colorbar. These orbits are corresponding to a frozen condition of $\Omega+\omega-\lambda_S = 0$, therefore they are characterized by an apogee that maintains its location always in the direction of the Sun [14]. Indeed, for a mission that studies the geomagnetic tail, elliptical, low-inclined orbits would be ideal, with a perigee around 5 Earth radii and apogee going from 5 to 30 Earth radii[4]. The lower the inclination and the higher is the area-to-mass ratio (i.e., the higher is the sail area considering

[4]See http://geo.phys.spbu.ru/~tsyganenko/modeling.html

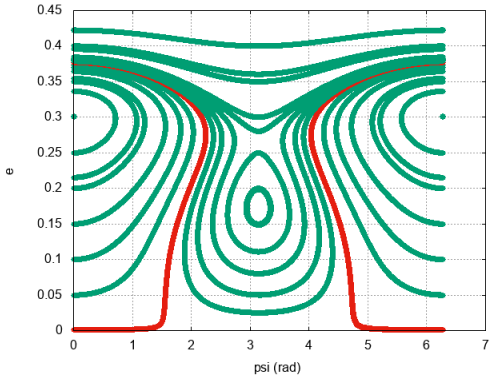

Figure 12: Phase portrait corresponding to Λ computed at $a = 7578$ km, $e = 0.001$, $i = 69.08°$, assuming that only resonance 4 dominates the dynamics and $A/m = 1$ m^2/kg.

Table 2: For each resonance j, assuming $a = 7578$ km, $A/m = 1$ m^2/kg and $e_0 = 0.001$ at the initial epoch, we display the value $\Lambda/\sqrt{\mu}$ (in km$^{1/2}$ units), corresponding to the initial inclination i_0, and the maximum eccentricity e_{max} that can be achieved starting from ψ_0 giving the steepest eccentricity increase, together with the corresponding phase ψ_{max} (rad) and time t_{max} (years).

j	ψ_0	i_0	$\Lambda/\sqrt{\mu}$	ψ_{max}	e_{max}	t_{max}
1	$\pi/2$	40.62°	-20.97	0	0.425	19.05
2	$3\pi/2$	77.92°	-105.27	π	0.112	12.00
3	$\pi/2$	58.53°	45.44	π	0.081	19.44
4	$3\pi/2$	69.08°	31.08	0	0.377	78.13
5	$\pi/2$	52.46°	-34.01	0	0.055	65.69
6	$3\pi/2$	68.96°	-118.3	π	0.027	81.70

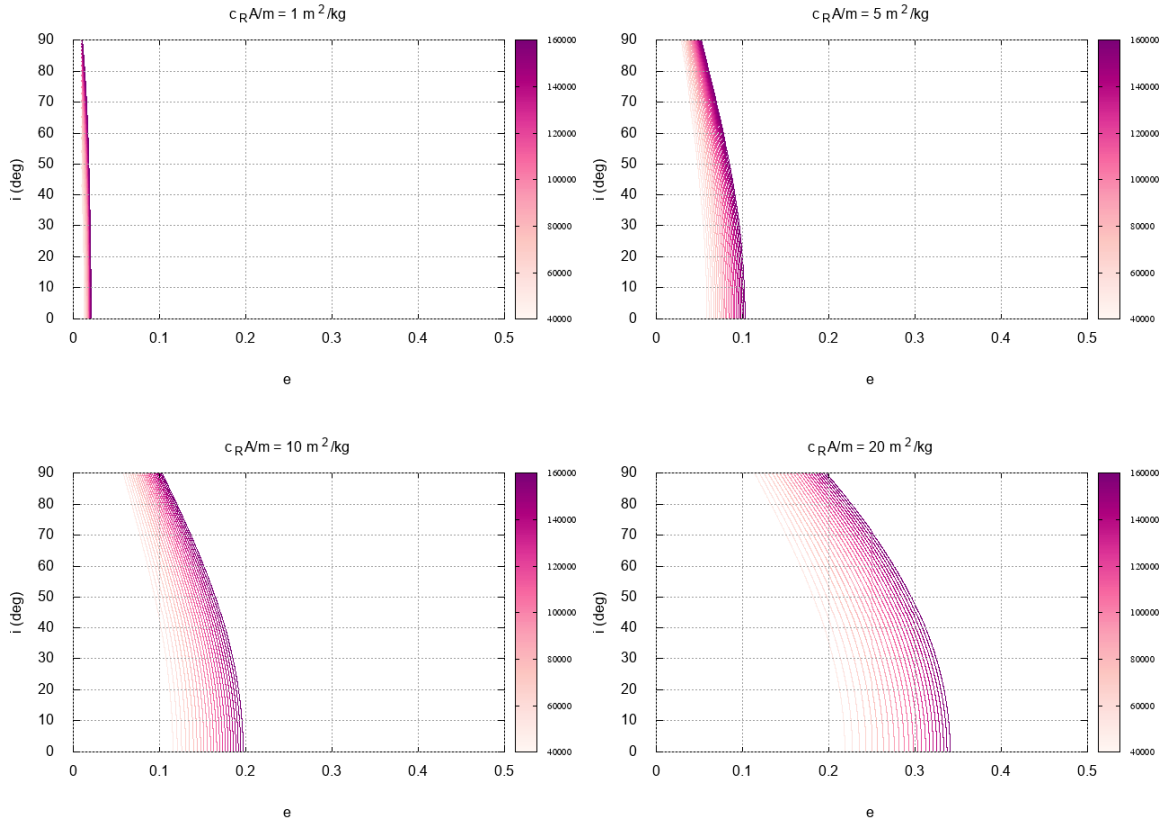

Figure 13: Equilibria location for resonance 1 (anti-heliotropic orbits) for different values of semi-major axis and area-to-mass ratio. Top-left: $A/m = 1$ m^2/kg, Top-right: $A/m = 5$ m^2/kg, Bottom-left: $A/m = 10$ m^2/kg, Bottom-right: $A/m = 20$ m^2/kg.

the same spacecraft mass), the more a stable anti-heliotropic orbit can be maintained with higher eccentricity. Therefore a solar sail would be ideal for this mission [12, 13, 14]. Alternatively also condition corresponding to libration around these equilibria point could be selected for this purpose.

4. Conclusions

In this work, we have presented the three-dimensional singly-averaged equations of motion corresponding to the perturbation due to the solar radiation pressure coupled with the oblateness effect. We have shown how the description of the dynamics can be reduced to a differential system of two independent variables and we have linked the concept of resonance with the one of equilibrium point for the aforesaid system.

This description proves to be a fundamental tool to design deorbiting strategy at the end-of-life, but also to design orbits for operational purposes. Here we have shown possible applications for large constellations in LEO and for geomagnetic tail observations, but other applications are foreseen in the future.

Acknowledgements

Part of this work is funded through the European Commission Horizon 2020, Framework Programme for Research and Innovation (2014-2020), under the ReDSHIFT project (grant agreement n. 687500). The authors would like to acknowledge Ioannis Gkolias for the useful discussions.

References

[1] P. Musen, The influence of the solar radiation pressure on the motion of an artificial satellite, J. Geophys. Res. 65 (1960), 1391-1396.

[2] G. E. Cook, Luni-Solar Perturbations of the Orbit of an Earth Satellite, Geophys. J. Roy. Astron. Soc. 6 (1962), 271-291.

[3] S. Hughes, Satellite orbits perturbed by direct solar radiation pressure: General expansion of the disturbing function, Planet Space Sci. 25 (1977), 809-815.

[4] S. Breiter, Lunisolar apsidal resonances at low satellites orbits, Cel. Mec. Dyn. Astron. 74 (1999), 253-274.

[5] S. Breiter, Lunisolar resonances revisited, Cel. Mec. Dyn. Astron. 81 (2001), 81-91.

[6] A. V. Krivov, L. L. Sokolov and V. V. Dikarev, Dynamics of Mars-Orbitting Dust: Effects of Light Pressure and Planetary Oblateness, Cel. Mec. Dyn. Astron. 63 (1996) 313-339.

[7] D. P. Hamilton, A. V. Krivov, Circumplanetary Dust dynamics: effects of solar gravity, radiation pressure, planetary oblateness, and electromagnetism, Icarus 123 (1996), 503-523.

[8] A. V. Krivov, J. Getino, Orbital evolution of high-altitude balloon satellites, Astron.Astrophys. 318 (1997), 308-314.

[9] C. Colombo, C. Lücking, C. R. McInnes, Orbital Dynamics of High Area-to-Mass Ratio Spacecraft with J_2 and Solar Radiation Pressure for Novel Earth Observation and Communication Services, Acta Astronaut. 81 (2012), 137-150.

[10] C. Colombo, C. R. McInnes, Constellations of Inclined Heliotropic Orbits for Enhanced Coverage, IAC-12.C1.4.12., 63rd International Astronautical Congress, Naples, Italy, 2012, 1-5 October.

[11] D. Lantukh, R. P. Russell, S. Broschart, Heliotropic orbits at oblate asteroids: balancing solar radiation pressure and J_2 perturbations, Cel. Mec. Dyn. Astron. 121 (2015), 171-190.

[12] T. Oyama, H. Yamakawa, Y. Omura, Orbital dynamics of solar sails for geomagnetic tail exploration, J. Guid. Contr. Dynam. 45 (2008), 316-323.

[13] C. R. McInnes, M. Macdonald, V. Angelopolous, D. Alexander, Geosail: exploring the geomagnetic tail using a small solar sail, J. Spacecr. Rockets 38 (2001), 622-629.

[14] T. Luo, M. Xu, C. Colombo, Dynamics and Control of High Area-to-Mass Ratio Spacecraft and Its Application to Geomagnetic Exploration, Acta Astronaut. 145 (2018), 424-437.

[15] C. Colombo, C. R. McInnes, Orbit design for future SpaceChip swarm missions in a planetary atmosphere, Acta Astronaut. 75 (2012), 25-41.

[16] A. Wittig, C. Colombo, R. Armellin, Long-term density evolution through semi-analytical and differential algebra techniques, Cel. Mec. Dyn. Astron. 128 (2017), 435-452.

[17] C. Lücking, C. Colombo, C. R. McInnes, A Passive Satellite Deorbiting Strategy for Medium Earth Orbit Using Solar Radiation Pressure and the J2 Effect, Acta Astronaut. 77 (2012), 197-206.

[18] C. Lücking, C. Colombo, C. R. McInnes, Solar Radiation Pressure-Augmented Deorbiting: Passive End-of-Life Disposal from High-Altitude Orbits, J. Spacecr. Rockets 50 (2013), 1256-1267.

[19] C. Colombo, de Bras de Fer T., Assessment of passive and active solar sailing strategies for end-of-life re-entry, IAC-16-A6.4.4., 67th International Astronautical Congress, Guadalajara, Mexico, 2016, 26-30 September.

[20] E. M. Alessi, G. Schettino, A. Rossi and G. B. Valsecchi, Natural Highways for End-of-Life Solutions in the LEO Region, Cel. Mec. Dyn. Astron. 130 (2018), 34.

[21] E. M. Alessi, G. Schettino, A. Rossi, G. B. Valsecchi, Solar radiation pressure resonances in Low Earth Orbits, Mon. Not. R. Astron. Soc. 473 (2018), 2407?2414.

[22] J. Daquin, A. J. Rosengren, E. M. Alessi, F. Deleflie, G. B. Valsecchi, A. Rossi, The dynamical structure of the MEO region: long-term stability, chaos, and transport, Celest. Mech. Dyn. Astron. 124 (2016), 335-366.

[23] G. Schettino, E. M. Alessi, A. Rossi, G. B. Valsecchi, A frequency portrait of Low Earth Orbits, Cel. Mec. Dyn. Astron. (2018), submitted.

[24] C. Colombo, A. Rossi, F. Dalla Vedova, A. Francesconi, C. Bombardelli, J. L. Gonzalo, P. Di Lizia, C. Giacomuzzo, S. Bayajid Khan, R. Garcia-Pelayo, V. Braun, B. Bastida Virgili, H. Krag, Effects of passive de-orbiting through drag and solar sails and electrodynamic tethers on the space debris environment, IAC-18-A6.2.10., 69th International Astronautical Congress, Bremen, Germany, 2018, 1-5 October.